



HAL
open science

A revised 1D equivalent model for the determination of incident photon flux density in a continuous-flow LED-driven spiral-shaped microreactor using the actinometry method with Reinecke's salt

Robbie Radjagobalou, Victoria Dias da Silva Freitas, Jean-François Blanco, Fabrice Gros, Jeremy Dauchet, Jean-François Cornet, Karine Loubière

► To cite this version:

Robbie Radjagobalou, Victoria Dias da Silva Freitas, Jean-François Blanco, Fabrice Gros, Jeremy Dauchet, et al.. A revised 1D equivalent model for the determination of incident photon flux density in a continuous-flow LED-driven spiral-shaped microreactor using the actinometry method with Reinecke's salt. *Journal of flow chemistry*, 2021, pp.0. 10.1007/s41981-021-00179-w . hal-03342383

HAL Id: hal-03342383

<https://hal.science/hal-03342383v1>

Submitted on 1 Oct 2021

HAL is a multi-disciplinary open access archive for the deposit and dissemination of scientific research documents, whether they are published or not. The documents may come from teaching and research institutions in France or abroad, or from public or private research centers.

L'archive ouverte pluridisciplinaire **HAL**, est destinée au dépôt et à la diffusion de documents scientifiques de niveau recherche, publiés ou non, émanant des établissements d'enseignement et de recherche français ou étrangers, des laboratoires publics ou privés.







Open Archive Toulouse Archive Ouverte (OATAO)

OATAO is an open access repository that collects the work of Toulouse researchers and makes it freely available over the web where possible

This is an author's version published in: <http://oatao.univ-toulouse.fr/28085>


Official URL: <https://doi.org/10.1007/s41981-021-00179-w>

To cite this version:

Radjagobalou, Robbie  and Dias da Silva Freitas, Victoria  and Blanco, Jean-François  and Gros, Fabrice and Dauchet, Jeremy and Cornet, Jean-François and Loubière, Karine  *A revised 1D equivalent model for the determination of incident photon flux density in a continuous-flow LED-driven spiral-shaped microreactor using the actinometry method with Reinecke's salt.* (2021) Journal of Flow Chemistry. ISSN 2062-249X

Any correspondence concerning this service should be sent to the repository administrator: tech-oatao@listes-diff.inp-toulouse.fr

A revised 1D equivalent model for the determination of incident photon flux density in a continuous-flow LED-driven spiral-shaped microreactor using the actinometry method with Reinecke's salt

Robbie Radjagobalou¹ · Victoria Dias Da Silva Freitas¹ · Jean-François Blanco¹ · Fabrice Gros² · Jérémy Dauchet² · Jean-François Cornet² · Karine Loubiere¹ 

Abstract

Continuous-flow microstructured technologies are now recognized as promising alternatives to batch processing for organic photochemistry, especially when light emitting diodes (LEDs) are employed as light sources. To evaluate and optimize productivity and energetic efficiency, the knowledge of the incident photon flux density is crucial. In this context, the objectives of the present work are dual: first, to transfer the classical actinometry method with Reinecke's salt to a continuous-flow LED-driven spiral-shaped reactor and second, to propose a revised one-dimensional equivalent model for the accurate determination of the incident photon flux density in this microreactor. Experimental measurements were carried out under controlled conditions. The effects of the spectral domain and radiant power emitted, the tubing length, the presence of gas-liquid Taylor flow, and the material of the support plate were especially investigated. An expression was established for the revised one-dimensional Cartesian model, taking into account the diffuse emission of the LED array and the reflection induced by the material of the plate in which the tubing was inserted (i.e. the reflection by the backside of the microreactor wall). In this way, the incident photon flux density could be estimated with an acceptable level of accuracy, which was not the case if the usual 1D model was applied (collimated emission and no reflection).

Keywords Flow photochemistry · Actinometry · Reinecke's salt · Modelling · Diffuse emission

Introduction

Photochemistry is now recognised as an indispensable synthetic pathway for sustainable chemistry [1–5], making it possible to shorten multistep syntheses of complex molecules or

to access novel molecular structures [6]. Nevertheless, although promising research has been done by academics, photochemistry is not widely implemented at an industrial scale. At present, it is mostly applied by chemical companies to produce intermediate and/or fine chemicals and by companies manufacturing basic or final products. Over the past two decades, continuous-flow microstructured technologies have become alternatives to batch processing for small-scale production plants (below a few tons per year). Due to the small dimensions of channels or tubes (a few tens of μm to a few mm), their suitability for organic photochemistry was quickly demonstrated [7–9], as such microreactors offer short light penetration distances and large irradiated specific areas while ensuring continuous removal of photoproducts from the irradiation zone, safer conditions, efficient transport phenomena and compact dimensions [10]. The integration of LEDs as light sources in these technologies additionally provides new solutions to select the most appropriate emission spectrum and to tune the emitted radiant power according to the reaction kinetics needed. For example, by means of a continuous-

Highlights

- Knowledge of the incident photon flux is essential for any design of a continuous flow microstructured photoreactor.
- The actinometry method with Reinecke's salt was successfully transferred to a continuous flow LED driven microreactor.
- By establishing a revised 1D Cartesian model, the incident photon flux densities could be determined with good accuracy.

✉ Karine Loubiere
Karine.Loubiere@ensiacet.fr

¹ Laboratoire de Génie Chimique (LGC), Université de Toulouse, CNRS, INPT, UPS, 4 allée Emile Monso, CS 84234, 31 432 Toulouse, France

² Université Clermont Auvergne, Clermont Auvergne INP, CNRS, Institut Pascal, F 63000 Clermont Ferrand, France

flow LED-driven microreactor, Haas et al. (2020) recently presented a systematic wavelength screening study with the perfluorobutylation of 2-methylindole as a test reaction, and demonstrated the advantages of LEDs and the associated discrete emission bands for triggering photochemical processes [11]. Their higher electrical yields, longer lifetimes and lower cooling requirements in comparison to mercury lamps also lead to energy savings [12].

To scale up (or down) any photoreactors, it is essential to know the incident photon flux density. Generally noted q_0 ($\text{mol}_{\text{photon}} \cdot \text{m}^{-2} \cdot \text{s}^{-1}$), it is defined as the amount of photons per unit of time and of surface area arriving at the *inner* surface of the optical walls of the reactor. This constitutes the boundary condition required to model the photoreactor, whatever the complexity of the chosen model. As the kinetic rate of any photochemical reaction is directly proportional to the incident photon flux, the latter parameter characterizes the fixed input energy rate and indicates the maximum performance of a given photoreactor in terms of volumetric production rates and energy efficiencies [10, 13, 14].

Generally, (i) the photon flux emitted by most light sources (e. g. mercury lamps) is inhomogeneous on the reactor's surface and (ii) the light transmission for all the surrounding parts of the reactor is not easy to integrate, which makes the determination of the value of q_0 difficult. In macro-scale photoreactors, direct measurements using radiometers or quantum sensors can be carried out on the inner side of the optical walls. However, this cannot be applied in microreactors since their dimensions are smaller than those of the sensor. An efficient alternative is to determine the mean incident photon flux, in other words the photon flux integrated over the whole irradiated surface of the reactor, by using a chemical actinometer. This method involves a simple photochemical reaction with a known quantum yield [15, 16], and consists of two consecutive steps: firstly, the variation of the actinometer concentration with the irradiation time is measured experimentally and, secondly, q_0 is obtained by fitting the experimental concentrations with a model coupling radiative transfer and photoreaction.

Although this method is well-established in large-scale (batch) photochemical reactors, few works have attempted to implement actinometry in microreactors, since flow photochemistry remains a young scientific field [9] and small dimensions can involve technical constraints (high pressure drops to achieve short residence times, clogging by actinometer precipitation, etc) [17]. The work of Aillet et al. [18] pioneered the first use of actinometry in microreactors. A classical actinometer in the UV domain, potassium ferrioxalate [19], was implemented in two different microphotoreactors (capillary-tower and spiral-shaped), irradiated by either a polychromatic or a monochromatic light source. A 1D Cartesian equivalent model considering a collimated emission, the partial absorption of photons

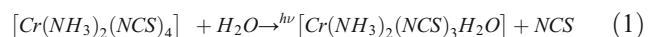
through the reactor depth and, if required, the polychromatic character of the light source and the dependence of the actinometer properties on the wavelength, was then formulated to describe the variation of the actinometer conversion with the irradiation. Later, Wriedt et al. [20], using the same actinometer and the same modelling, proposed a new experimental protocol in which continuous measurements were replaced by pulsed measurements, and successfully applied it in a multilayer capillary microreactor. In 2017, El Achi et al. [21] implemented actinometry using azobenzene at 365 nm inside a microphotoreactor. Different solvents and irradiation powers were assessed and NMR spectroscopy analysis was used to monitor the rate of the photoisomerization. To determine the incident photon flux, they derived the kinetic equation based on the Beer-Lambert law that depended on the proportion of isomers formed. It was applicable for concentrated solutions and led to reliable actinometrical measurements without the need to know the quantum yield nor the extinction coefficient of (Z)-azobenzene. When the light source emission switches towards the visible domain, the incident photon flux should be quantified using appropriate actinometers, such as mesodiphenylhelianthrene [16, 22], a diarylethene derivative actinometer (1,2-bis(5-(4-ethynylphenyl)-2-methylthiophen-3-yl)perfluorocyclopentene) synthesized in the laboratory [23], Reinecke's salt [14, 16, 24], Aberchrome 540 [16, 25] or 1,9-diphenylanthracene (DPA) [26]. Recently, Roibu et al. [27] proposed a new actinometer (between 480 and 620 nm) based on the photoisomerization reaction of a diarylethene derivative from its closed to open form. The related experimental protocol for actinometrical measurements was implemented in microreactors with good reproducibility. These authors presented an analytical expression to calculate the photon flux, based on a Beer-Lambert law (collimated light) accounting for the polychromaticity of the light source. In addition, they established an experimental methodology to determine the average light path length in microreactors using actinometrical measurements.

In this context, the objectives of the present work are dual: first, to transfer the classical actinometry method with Reinecke's salt to a continuous-flow LED-driven spiral-shaped reactor, and, secondly, to propose a revised one-dimensional equivalent model in order to accurately determine the incident photon flux density in this microreactor. Experimental measurements were first carried out under controlled conditions. The effects of the operating conditions, such as the spectral domain and the radiant power emitted, the tubing length, the presence of gas-liquid Taylor flow, or the material of the base plate, on the concentration of thiocyanate anion (NCS⁻) were especially investigated. Then, the one-dimensional Cartesian model (infinite parallel plates), classically used to extract the incident photon flux density from the experimental data was upgraded so as to describe the features of the LED-driven spiral-shaped microreactor

more faithfully. The proposed modifications took into account (1) the diffuse emission of the present LED array (and not a collimated emission described in the literature) and (2) the contribution of the photon reflection induced by the base plate in which the tubing was inserted. Finally, the classical model (which considered a collimated emission and no reflection) and the proposed revised model were confronted to the experimental data. In particular, the results demonstrated that, by using the proposed revised model, the incident photon flux densities could be determined with a good accuracy whatever the operating conditions, whereas the common 1D model (collimated emission, without reflection) led to large overestimations of the incident photon flux density.

Experimental section

Reinecke's salt remains the most popular actinometer in the visible domain. It involved the following chemical equation:



Eq. (1) shows that the rate of photodissociation of the salt is equal to the rate of production of the thiocyanate anion, NCS^- , making it possible to monitor the kinetics by dosing NCS^- . It is noteworthy that

- the absorption of the Reinecke's salt is maximal at 525 nm,
- the associated quantum yield is relatively stable ($\phi = 0.29 \pm 0.02$) in the range of 400–700 nm when the pH of the solution is between 3 and 5 [28],
- the absorption of the by-product, $[Cr(NH_3)_2(NCS)_3(H_2O)]$, is of the same order of magnitude as that of the actinometer, and
- working at low conversions (below 30%) is recommended to limit the occurrence of secondary reactions (i. e. the substitution of more than one NCS^- ligand by a molecule of water) [24].

In the present work, the revised experimental procedure recently proposed by Radjagobalou et al. [29] was applied, which consists in substituting nitric acid for the perchloric acid. More details can be found in the Section S.1 of the Supplementary Material. Note that, for all the experiments, the initial concentration of Reinecke's salt was 15 mol.m^{-3} .

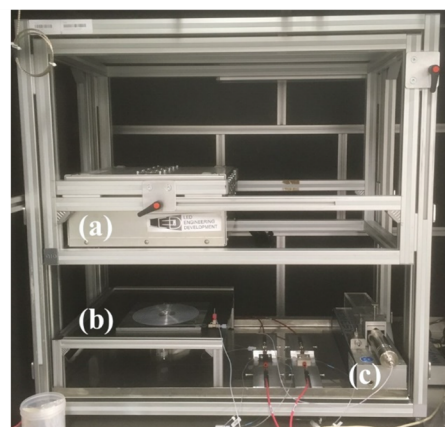
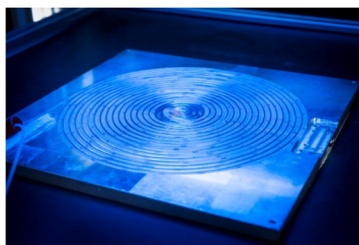
Actinometry experiments were carried out under continuous-flow conditions within the LED-driven microreactor used by Radjagobalou et al. [30] for the photooxygenation of α -terpinene in presence of Bengal rose anchored polymer colloids.

As shown in Fig. 1, this microreactor consisted of FEP tubing fixed in a channel carved in a flat plate of either aluminium or polymethylmethacrylate (PMMA), and wound into an Archimedean spiral [31, 32]. Tubing with an internal diameter, d_i , equal to either 0.5 mm or 1 mm (the corresponding external diameter being 1.58 mm or 3.2 mm) was used. Different lengths of tubing, L_t (m), were also implemented: 2.4, 4 and 6 m for d_i equal to 0.5 mm, and 1.2, 3 and 5 m for d_i equal to 1 mm. More details about the different geometrical configurations (noted microreactors N°1, N°2 and N°3) can be found in Section S.2 of the Supplementary Material.

The pumping system was a high-pressure syringe pump in stainless steel (neMESYS High-Pressure Module, Cetoni®). The volume of syringe was 100 mL. The flowrate of the actinometer solution varied from a few mL.min^{-1} to tens of mL.min^{-1} , leading to residence times, τ (s), of the order of a few seconds. The tubing sections located out of the spiral were covered by aluminium foil so as to set the irradiation time equal to the residence time inside the microreactor. The samples were collected in an amber glass and immediately analysed to prevent any change of the reactional medium between the collection of the sample and its analysis.

The spiral-shaped microreactor was illuminated by a purpose-built visible-LED array manufactured by the Led Engineering Development company (Montauban, France) (see Fig.1). Compared to standard white LEDs, this advanced LED array consisted of more than 1500 individual LEDs of

Fig. 1 Continuous flow LED driven spiral shaped microreactor. Left image: Archimedean spiral geometry of the tubing fixed in a channel carved in a flat plate of aluminium (Jean Claude Moschetti, LGC, CNRS Photothèque). Right image: experimental set up including (a) the LED panel, (b) the microreactor and (c) the pumping system



ten different types. It thus (i) had an emission spectrum in the whole visible domain that was flatter than the usual one obtained from visible light LED (characterized by a narrow peak around 450 nm in the blue region and a wide peak around 620 nm), (ii) enabled a specific spectral domain to be chosen in the visible and, (iii) permitted modulation of the emitted radiant power. In the present study, three emission modes were considered: (1) yellow light [450 nm–600 nm], (2) blue light [400 nm–500 nm], and (3) green light [520 nm–540 nm]. The spectral domain reported in brackets corresponds to the one where at least 70% of the emitted photons were located. For each mode, three or four levels of radiant energy densities (noted q_r ($\text{W}\cdot\text{m}^{-2}$)), could be chosen, varying from 19 to 52 $\text{mW}\cdot\text{cm}^{-2}$. More details are given in Section S.3 of the Supplementary Material.

Results and discussion

Experimental investigations

Influence of the emission mode and the emitted radiant power

Figure 2 presents the variation of the concentration of NCS with the residence time for the yellow light mode and at different radiant energy densities received at the surface of the microreactor (q_r). This set of experiments was carried out using microreactor N°3 $\{d_i = 1 \text{ mm}; L_t = 1.2 \text{ m}\}$ and the aluminium base plate. Special care was taken to maintain concentrations of NCS below $4.5 \text{ mol}\cdot\text{m}^{-3}$ which corresponded to a conversion of 30%, as recommended by Rochatte et al. [24] in order to avoid secondary reactions between the by-product $[\text{Cr}(\text{NH}_3)_2(\text{NCS})_3\text{H}_2\text{O}]$ and water.

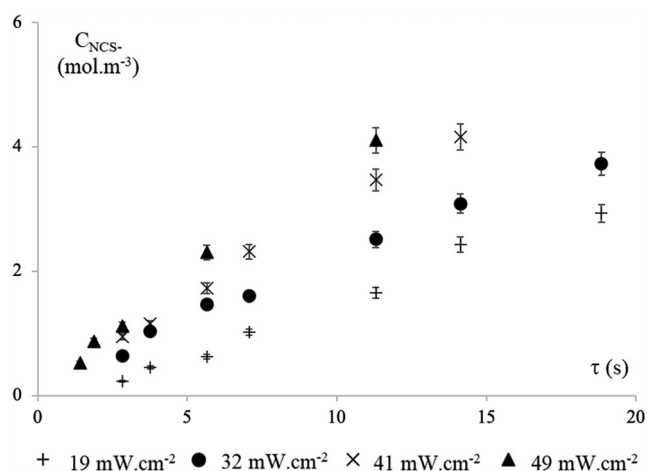


Fig. 2 Variation of the concentration of NCS ($\text{mol}\cdot\text{m}^{-3}$) with the residence time (s) for the yellow light ([450 nm 600 nm]) at different radiant energy densities received at the surface of the microreactor q_r ($\text{mW}\cdot\text{cm}^{-2}$). The microreactor N°3 $\{d_i = 1 \text{ mm}; L_t = 1.2 \text{ m}\}$ and the base plate in aluminium were used

It can first be observed that the residence times required to maintain conversions below 30% were small (below one minute), and could even fall to a few seconds. In addition, whatever the radiant power, an increase in emitted radiant energy densities led to an almost proportional increase in the slope of the curves C_{NCS} versus τ .

The same conclusions could be drawn from the experiments carried out with the blue and green light modes, as reported in the Supplementary Material (section S.4).

Influence of the tubing length

In the case where the spatial distribution of the photon flux density (q_r) received at the surface of the microreactor is not perfectly homogeneous, the incident photon flux density (q_0), extracted from actinometry experiments using an ad hoc model, could vary according to the microreactor's configuration (i.e. to the length of wound tubing). This point is particularly important in the perspective of implementing photochemical reactions under controlled irradiation conditions. If a spatial heterogeneity of incident photon flux densities existed, it would lead to different reaction rates along the tube (all other parameters being considered constant), which would make the kinetic study much more complex. To investigate this issue, specific experiments were carried out by varying the tubing length of the microreactor, while keeping the emission mode and the emitted radiant energy density constant.

Figure 3 represents the associated results for the yellow light at $q_r = 32 \text{ mW}\cdot\text{cm}^{-2}$ (microreactors N°1, N°2 or N°3 with $d_i = 1 \text{ mm}$ and the base plate in aluminium).

It can be seen that, the variations of the concentration of NCS with τ remained similar for all the tubing lengths, when the experimental uncertainties were taken into account. The same trends were obtained with the blue and green light modes, as reported in the Supplementary Material (section S.4). Therefore, even if a slight heterogeneity in the spatial distribution of the photon flux density could exist at the surface of the microreactor, the kinetic rate of the actinometry reaction was not affected by it. In other words, the number of photons absorbed per unit of irradiated surface and per unit of time did not depend on the length of the reactor. Thus, it is reasonable to assume that the photon flux density emitted by the designed LED panel was homogenous over the whole surface of the microreactor. Another consequence is that, for a given q_0 , working with short or long tubing is similar from a radiative transfer point of view, which is particularly interesting for achieving very small residence times (few seconds) while maintaining an acceptable level of pressure drop.

Influence of the material of the base plate

In this new set of experiments, the nature of the base plate in which the tubing was inserted was specifically investigated. As the reflection coefficient of the aluminium base plate

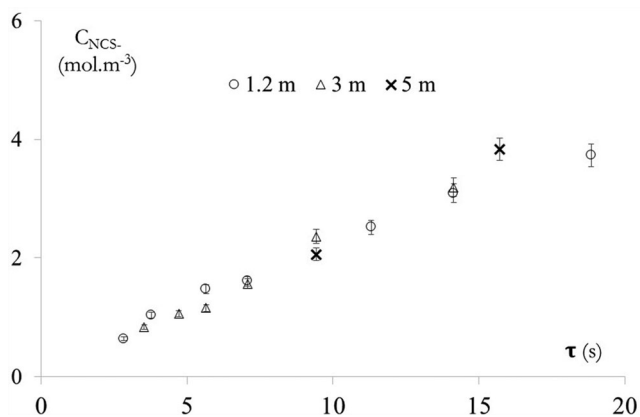


Fig. 3 Variation of the concentration of NCS (mol.m^{-3}) with the residence time (s) for different tubing lengths with the yellow light ([450 nm–600 nm]) at $q_r = 32 \text{ mW.cm}^{-2}$. The microreactors N°1, N°2 and N°3 with $d_i = 1 \text{ mm}$ and the base plate in aluminium were used

differs from that of the one manufactured in PMMA, the question arises as to whether this phenomenon will affect the variation of the NCS concentration with residence time or not.

To answer this question, experiments were carried out by using both types of base plate (aluminium versus PMMA) and the microreactors N°1, N°2 and N°3 with $d_i = 0.5 \text{ mm}$ irradiated by the yellow light mode ([450 nm–600 nm]) at $q_r = 32 \text{ mW.cm}^{-2}$. Figure 4 represents the concentration of NCS as a function of the residence time in these operating conditions. Firstly, as previously observed for the aluminium plate, a change in the length of the tubing does not affect the reaction rate when the PMMA plate is used. Secondly, using the aluminium plate instead of the PMMA plate affects the reaction rate; at identical irradiation times, lower concentrations of NCS are obtained with the PMMA plate. Such a result points out that the radiative properties of the material constituting the base plate in which the tubing is fixed have a significant effect on the radiative transfer inside the microreactor, namely on the number of photons absorbed. If the absorption of the incident photon flux in the reaction medium is not complete (optically thin medium), the photons transmitted over the back side of

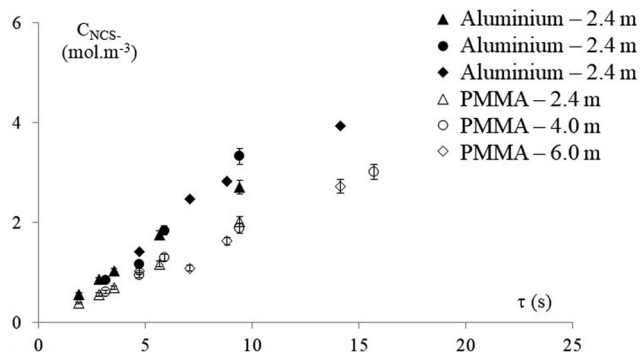


Fig. 4 Variation of the concentration of NCS (mol.m^{-3}) with the residence time (s) whether the base plate used is made of aluminium or PMMA, and for different tubing lengths (yellow light mode ([450 nm–600 nm]) at $q_r = 32 \text{ mW.cm}^{-2}$, $d_i = 0.5 \text{ mm}$)

the tubing wall encounter the material of the base plate, and may be reflected and absorbed in the reaction medium on their way back. The higher the reflectivity, the higher the number of photons absorbed is. Therefore, lower concentrations of NCS were recorded with the PMMA plate (low reflectivity) in comparison with those of aluminium plate (high reflectivity).

The fact that the base plate affects the reaction rate indicates that a significant amount of incident photons is transmitted through the microreactor and reaches the base plate. In standard actinometry, all the incident radiations are absorbed and thus this effect does not occur [12, 16]. This is the reason why the determination of the incident photon flux density in a microreactor requires to develop a specific radiative transfer model, while it is not necessary in standard photoreactors.

Influence of gas-liquid segmented flows

When two-phase photochemical reactions are performed in continuous-flow microreactors, Taylor flows, also called slug flows, are generally promoted. The pattern consists of a segmented flow in which bubbles or droplets (dispersed phase) are regularly spaced by liquid slugs and a thin lubrication film is formed between the channel wall and the bubbles (Fig. 5). The features of this flow pattern intensify the mixing and the interfacial mass transfer, in comparison with those in conventional multiphase reactors [33]. For example, when carrying out the sensitized photooxygenation of α -terpinene in the E-Series UV-150 Vapourtec® reactor, Radjagobalou et al. [34] demonstrated how the reaction performances could be affected by the mixing characteristics in the liquid slugs, all other parameters being kept constant (especially the stoichiometry ratio and the gas fraction). Other authors have pointed out that using Taylor flows with an inert phase (i.e. an unreactive phase) dispersed in the continuous phase could be a promising way to achieve higher and selective conversions in the case of photochemical reactions, such as the Paterno-Büchi photoreaction or the [2 + 2] photocycloaddition of cinnamate [35–38].

In this context, specific experiments were done to study the influence of a segmented flow when the photodissociation of the Reinecke's salt was operated, which is a perfectly known photochemical reaction. For that, nitrogen bubbles were generated inside the microreactor, so as to generate a Taylor flow in which the liquid slugs consisted of the Reinecke's salt solution. The spatial distribution of gas and liquid phases inside the tube was controlled by the volumetric ratio, noted R_V (-):

$$R_V = \frac{Q_G}{Q_L} \quad (2)$$

where Q_G ($\text{m}^3.\text{s}^{-1}$) and Q_L ($\text{m}^3.\text{s}^{-1}$) are the gas and liquid flow rates, respectively. Note that the amount of nitrogen introduced into the microreactor can also be expressed in terms of gas fraction, β_G (-), as:

$$\beta_G = \frac{Q_G}{Q_L + Q_G} \quad (3)$$

From Eq. 2 and Eq. 3, the two parameters are linked according to

$$\beta_G = \frac{R_V}{1 + R_V} \quad (4)$$

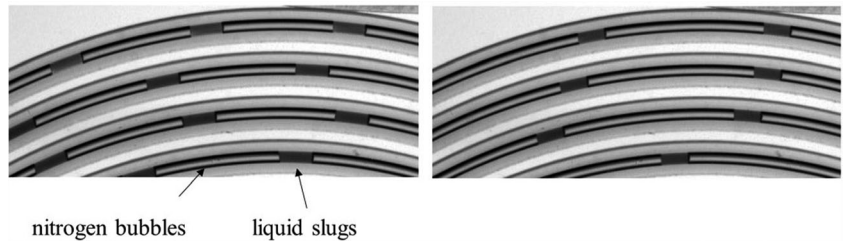
Figure 5 shows typical images of gas-liquid Taylor flows obtained in the spiral-shaped microreactor for the two configurations under test. The latter were performed with volumetric ratio, R_V , equal to 3 and 5, corresponding to gas fractions, β_G , equal to 75% and 83% respectively. In these cases, long bubbles and short liquid slugs were generated.

Figure 6 compares the variations of the concentration of NCS with residence time for a homogeneous flow (no nitrogen bubbles) and for two gas-liquid Taylor flows, corresponding to two values of R_V . Note that

- for two-phase flows, the residence time was estimated as the ratio between the reactor volume, noted V_R (m^3), and the total inlet volumetric flow rate ($Q_L + Q_G$),
- the experiments were carried out without changing the tubing length which means that, for a given residence time, an increase of R_V from 3 to 5 implied an adjustment of the gas and liquid flow rates while keeping the total flow rate (and thus the residence time) constant and making sure the two-phase flow remained stable.

Figure 6 shows that the variation of NCS concentration with the residence time is the same with Taylor flows (nitrogen bubbles/Reinecke's salt solution) and the homogeneous solution (Reinecke's salt solution only). Allowing for experimental uncertainties, the points are superimposed on each other. In addition, the change in the bubble length when R_V falls from 5 to 3 does not affect this variation. This result shows that the 3D effects can be neglected in the present operating conditions: the photoreaction within liquid films (between bubble body and walls), as well as photons entering slugs from the bubble rear and nose are negligible. It reinforces the proposal of this work to construct and use a 1D equivalent model for radiative transfer.

Fig. 5 Typical images of gas liquid Taylor flows obtained in the spiral shaped microreactor when $R_V = 3$ (left) and $R_V = 5$ (right)



Modeling investigations

Upgraded model

The revised experimental protocol of the Reinecke's salt actinometer was validated in a flat torus photoreactor operating in batch mode and irradiated by a quasi-collimated blue light LED panel ($\lambda = 457$ nm). In this case, it can be demonstrated that the analytical expression of the production of NCS during the irradiation time t is rigorously given by [28]:

$$\frac{dC_{\text{NCS}}}{dt} = \phi_R \bar{\kappa}_R C_R (1 - f_d) \cdot a_{\text{light}} \frac{q_0}{\bar{\kappa}_R \cdot C_R + \bar{\kappa}_P \cdot C_P} \left(1 - e^{-(\bar{\kappa}_R C_R + \bar{\kappa}_P C_P) \cdot \delta} \right) \quad (5)$$

where $\phi_R (-)$ is the quantum yield of the photodissociation of the Reinecke's salt, q_0 ($\text{mol}_{\text{photon}} \cdot \text{m}^{-2} \cdot \text{s}^{-1}$) is the incident photon flux density, C_R and C_P ($\text{mol} \cdot \text{m}^{-3}$) are the concentrations of the Reinecke's salt and of the by-product, $f_d (-)$ is the dark fraction in the volume which represents the fraction of volume that is non-irradiated, and $\bar{\kappa}_R$ and $\bar{\kappa}_P$ ($\text{m}^2 \cdot \text{mol}^{-1}$) are the averaged Napierian molar absorption coefficients of the Reinecke's salt and of the by-product defined by

$$\bar{\kappa}_i = \frac{\int_{\lambda_{\min}}^{\lambda_{\max}} \kappa_{i,\lambda} \cdot f_{\lambda}^{\text{LED}} \cdot d\lambda}{\int_{\lambda_{\min}}^{\lambda_{\max}} f_{\lambda}^{\text{LED}} \cdot d\lambda} \quad (6)$$

where f_{λ}^{LED} (nm^{-1}) is the density function of the light source at each wavelength λ .

Note that, in Eq. 5, a_{light} (m^{-1}) is the specific irradiated area defined by the ratio between the irradiated surface of the reactor, S_{light} (m^2), and the volume of the reactor, V_R (m^3).

The features of the LED-driven spiral-shaped microreactor are much more complex than those of the torus photoreactor: (i) the surface of the reactor (i.e. the wound tubing) is not flat, (ii) the base plate on which the tubing is fixed manufactured in aluminium can mainly reflect photons transmitted by the back side of the tubing wall, (iii) the light emission profile of the LED array was diffuse (see section S.3 of the Supplementary Material) and (iv) the flow was laminar (and therefore not perfectly mixed). Consequently, Eq. 5 is no longer suitable to identify the incident photon flux density (q_0) with an acceptable level of accuracy in the present device and needs to be upgraded. As a first step in this direction, this section proposes to modify the one-dimensional Cartesian modelling

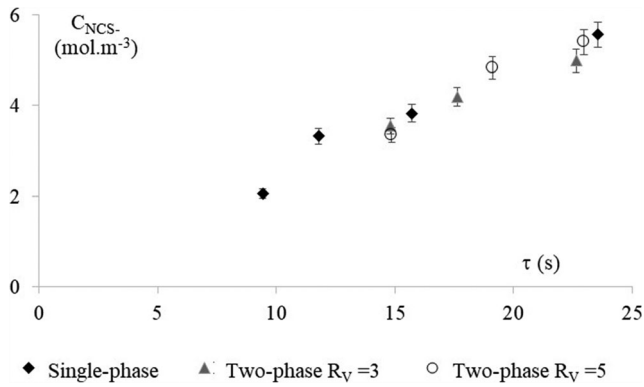


Fig. 6 Variation of the concentration of NCS (mol.m⁻³) with the residence time (s) for different flow patterns: single phase flow (no nitrogen bubble), two phase flows with $R_V = 3$ and $R_V = 5$. Operating conditions: yellow light ([450 nm – 600 nm]) at $q_r = 32 \text{ mW.cm}^{-2}$; microreactor N°3 with $d_f = 1 \text{ mm}$ ($L_r = 1.2 \text{ m}$) and base plate in aluminium

previously established in the flat torus photoreactor irradiated by a quasi-collimated photon source, so as to describe the radiative configuration of the LED-driven spiral-shaped microreactor more accurately. The modifications will consist in taking a diffuse emission into account (instead of a normal collimated one) and the contribution of the photon reflection induced by the plate in which the tubing is inserted.

First of all, considering a plug flow behaviour in the spiral-shaped microreactor, the mass balance in a volume element of the liquid phase can be rewritten as

$$\langle r_R \rangle = -Q_L \frac{dC_R}{dV} = \frac{dC_{NCS}}{d\tau} \quad (7)$$

where $\langle r_R \rangle$ (mol.m⁻³.s⁻¹) is the rate of the photodissociation of the Reinecke's salt averaged over the liquid cross-section (i.e. over the internal diameter, d_i) at a given residence time τ .

The local rate of photodissociation of the Reinecke's salt (i.e. defined at a given point within the liquid volume and at a given wavelength) is expressed as:

$$r_R = \phi_R e_R^a \quad (8)$$

where e_R^a (mol_{photon}.m⁻³.s⁻¹) is the absorption rate of photons per unit of time and unit of liquid volume. This spectral quantity is defined as:

$$e_R^a = \kappa_R C_R E \quad (9)$$

where E (mol_{photon}.m⁻².s⁻¹) is the irradiance determined by solving the radiative transfer equation.

Assuming linear thermokinetic coupling (i.e. ϕ_R does not depend on e_R^a), the average rate of the photodissociation over the liquid cross-section, $\langle r_R \rangle$, can be expressed as

$$\langle r_R \rangle = \phi_R \langle e_R^a \rangle = \phi_R \langle \kappa_R C_R E \rangle = \phi_R \kappa_R C_R \langle E \rangle \quad (10)$$

To solve this mass balance (Eq. 10 combined with Eq. 7), the mean irradiance $\langle E \rangle$ (mol_{photon}.m⁻².s⁻¹) must be

determined. To do this, the optical path length first needs to be considered. As shown in Fig. 7 and in Section S.5 of the Supplementary Material, the light path is complex due to the fact that light crosses several interfaces within the spiral-shaped microreactor. When penetrating inside the spiral-shaped microreactor, photons go through four interfaces successively, from air to the base plate in which the tubing is wound: air/FEP (interface n°1), FEP/reaction medium (interface n°2), reaction medium/FEP (interface n°4) and FEP/Plate (interface n°5). Each interface (or group of interfaces) is characterized by a reflection coefficient, ρ_i (-), the respective values of which are given in Section S.5 of the Supplementary Material.

When the reflection is taken into account, the calculation of $\langle E \rangle$ can be decomposed into two contributions: the incident radiation incoming from air that reaches the base plate, noted $\langle E \rangle_I$ (mol_{photon}.m⁻².s⁻¹), and the contribution of radiation reflected at the base plate that propagates upward and then the optical surface of the reactor (reflection), noted $\langle E \rangle_{II}$ (mol_{photon}.m⁻².s⁻¹). Since radiative transfer is a linear physics, those two contributions are simply added, as:

$$\langle E \rangle = \langle E \rangle_I + \langle E \rangle_{II} \quad (11)$$

In the Supplementary Material, the expressions for the mean irradiance $\langle E \rangle$, and thus of the subsequent mass balances, were established for a normal collimated emission (Section S.6) and for a diffuse emission (Section S.7). They are reported in Table 1. In both cases, the possible photon reflection induced by the base plate in which the tubing is inserted is taken into account, in particular by introducing the reflection coefficient of the interface n°6 (ρ_6) that combines both interfaces n°4 (reaction medium/FEP) and n°5 (FEP/plate) (see Fig. 7 and section S.5 of the Supplementary Material).

Contribution of the reflection phenomenon

Experimentally, it was observed that higher concentrations of NCS were achieved at a given irradiation time with an aluminium plate than with a PMMA one (Fig. 4). To understand this result, and to evaluate the contribution of the photon flux density reflected at the plate surface to the production rate of NCS, the modelling approach previously presented was used (Table 1). For this purpose, let us introduce the ratio, ζ (-), of the mean absorption rates of photons without reflection (i.e. when $\rho_6 = 0$) and with reflection (i.e. when $\rho_6 \neq 0$), that is to say when the aluminium plate is used. This ratio is expressed as

$$\zeta = \frac{\langle e_R^a \rangle_{\rho_6=0}}{\langle e_R^a \rangle_{\rho_6 \neq 0}} \quad (12)$$

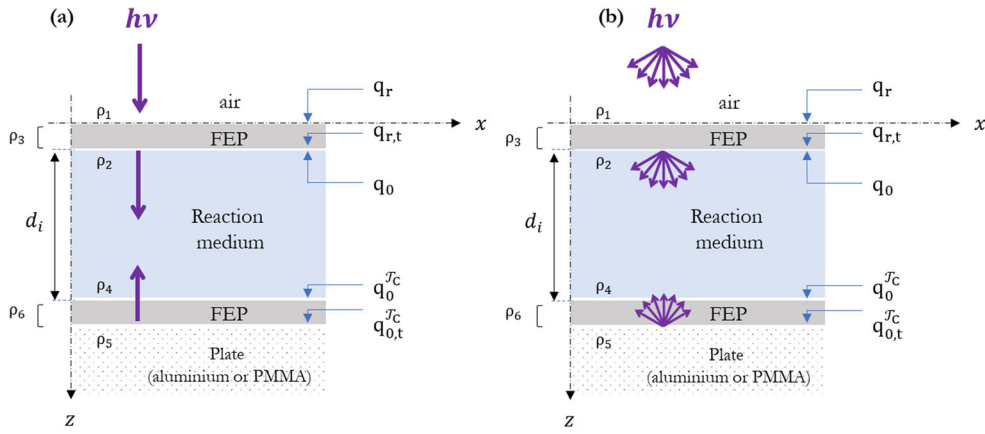


Fig. 7 Schematic representation of the different interfaces and the light path in the LED driven spiral shaped microreactor, for a normal collimated incidence (a) and for a diffuse incidence (b). The optical path length δ was assumed to be equal to the inner diameter of the tubing, d_i . q_r ($\text{mol}_{\text{photon}} \cdot \text{m}^{-2} \cdot \text{s}^{-1}$) is the photon flux density at the external wall of the FEP tubing located on the LED panel side. $q_{r,t}$ ($\text{mol}_{\text{photon}} \cdot \text{m}^{-2} \cdot \text{s}^{-1}$) is the photon flux density transmitted to the internal wall of the FEP tubing located on the LED panel side. q_0 ($\text{mol}_{\text{photon}} \cdot \text{m}^{-2} \cdot \text{s}^{-1}$) is the incident photon flux density. q_0^C, q_0^D ($\text{mol}_{\text{photon}} \cdot \text{m}^{-2} \cdot \text{s}^{-1}$) are the amounts of the

incident photon flux density that are not absorbed by the reaction medium and thus arrive at the internal side of the second FEP tubing wall. $q_{0,t}^C, q_{0,t}^D$ ($\text{mol}_{\text{photon}} \cdot \text{m}^{-2} \cdot \text{s}^{-1}$) are the amounts of the incident photon flux density transmitted by the back side of the wall of the FEP tubing located on the plate side. The indexes C and D refer to the model considering a collimated emission and a diffuse emission, respectively, and T to the probability of transmission of photons (see sections S.6 and S.7 of the Supplementary Material)

If $\zeta \rightarrow 1$, then the reflection of light can be considered as negligible. Using the equations reported in Table 1, it can be demonstrated that

- for a normal collimated emission:

$$\zeta = \frac{1}{1 + \rho_6 e^{(\bar{\kappa}_R C_R + \bar{\kappa}_P C_P) \delta}} \quad (13)$$

Table 1 Expressions for the mass balances depending on whether normal collimated emission or diffuse emission is considered in the modelling. $\mathcal{T}(\cdot)$ and $\mathcal{A}(\cdot)$ are the probabilities of transmission and absorption of photons, respectively. The indexes ‘‘C’’ and ‘‘D’’ refer to

the collimated and diffuse cases respectively. ρ_6 is the reflection coefficient of the interface n°6 that combines interfaces n°4 (reaction medium/FEP) and n°5 (FEP/plate) (see Fig.7, and section S.5 and Fig. S.7 of the Supplementary Material)

Normal collimated emission

$$\frac{dC_{\text{NCS}}}{dt} = \Phi_R \bar{\kappa}_R C_R \cdot (1 - f_d) a_{\text{light}} \frac{q_0}{\bar{\kappa}_{\text{tot}}} \mathcal{A}_C (1 + \rho_6 \mathcal{T}_C)$$

with

$$\mathcal{A}_C = 1 - \mathcal{T}_C = 1 - e^{-(\bar{\kappa}_{\text{tot}}) \delta}$$

and

$$\bar{\kappa}_{\text{tot}} = \bar{\kappa}_R C_R + \bar{\kappa}_P C_P$$

Diffuse emission

$$\frac{dC_{\text{NCS}}}{dt} = \Phi_R \bar{\kappa}_R C_R (1 - f_d) a_{\text{light}} \frac{q_0}{\bar{\kappa}_{\text{tot}}} \mathcal{A}_D (1 + \rho_6 \mathcal{T}_D)$$

with

$$\mathcal{A}_D = 1 - \mathcal{T}_D = F(\bar{\kappa}_{\text{tot}}) = 1 + \bar{\kappa}_{\text{tot}} \delta - 1 - e^{-\bar{\kappa}_{\text{tot}} \delta} + \bar{\kappa}_{\text{tot}} \delta^2 E_1 - \bar{\kappa}_{\text{tot}} \delta$$

and

$$\mathcal{T}_D = 1 - \bar{\kappa}_{\text{tot}} \delta e^{-\bar{\kappa}_{\text{tot}} \delta} - \bar{\kappa}_{\text{tot}} \delta^2 E_1 - \bar{\kappa}_{\text{tot}} \delta$$

with

$$\bar{\kappa}_{\text{tot}} = \bar{\kappa}_R C_R + \bar{\kappa}_P C_P$$

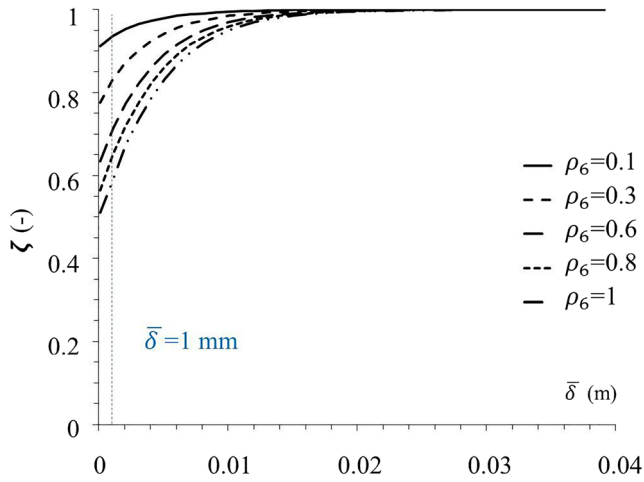


Fig. 8 Variation of the ratio $\zeta(\cdot)$ as a function of the characteristic optical path length $\bar{\delta}$ (m) and the reflection coefficient $\rho_6(\cdot)$ for the inlet condition chosen to implement the actinometry protocol in the spiral shaped microreactor ($C_{R,0} = 15 \text{ mol.m}^{-3}$; $C_{P,0} = 0$; $\bar{\kappa}_R \approx 14 \text{ m}^2.\text{mol}^{-1}$, leading to $\bar{\kappa}_{\text{tot}} = \bar{\kappa}_R.C_{R,0} = 210 \text{ m}^{-1}$), in the case where a diffuse emission is considered in the modelling

- for a diffuse emission:

$$\zeta = \frac{1}{1 + \rho_6 \left[\left(1 - \bar{\kappa}_{\text{tot}} \bar{\delta}\right) e^{\bar{\kappa}_{\text{tot}} \bar{\delta}} - \left(\bar{\kappa}_{\text{tot}} \bar{\delta}\right)^2 E_i\left(-\bar{\kappa}_{\text{tot}} \bar{\delta}\right) \right]} \quad (14)$$

Figure 8 reports the variations of the ratio ζ with the characteristic optical distance $\bar{\delta}$ and the reflection coefficient ρ_6 , in the case where a diffuse emission is considered in the modeling (Eq. 14). For these calculations, it was assumed that $C_{R,0} = 15 \text{ mol.m}^{-3}$ and $C_{P,0} = 0$, which corresponded to the condition at the reactor inlet when the actinometry protocol was implemented in the spiral-shaped microreactor. Note that, in the case of a normal collimated emission, the results were almost equal to those reported in Fig. 8.

Figure 8 reveals the strong dependence of the ratio ζ on the optical distance. For $\bar{\delta} = 0.025 \text{ m}$ (i.e. in the flat torus reactor used by Rochatte et al. [24] and Radjagobalou et al. [29]), the ratio ζ remains close to unity, whatever the type of emission. This means that, in this case, and more generally for $\bar{\delta} > 0.025 \text{ m}$, the reflection induced by the base plate can be assumed negligible. However, for $\bar{\delta} < 0.025 \text{ m}$, the contribution of the reflection becomes more and more pronounced ($\zeta < 1$) and increases with ρ_6 . In particular, it can be observed that, for $\bar{\delta} \approx 1 \text{ mm}$ (see Fig. 8), which corresponds to the inner diameter of the tubing, and when considering $\rho_6 > 0.6$ as for the aluminium plate [39], the contribution of the reflection is important since the ratio ζ falls to 0.7. In the spiral-shaped photoreactor, this would suggest that more photons could be absorbed by the Reinecke's salt per unit of volume and of time (higher $\langle e_R^a \rangle$) with the aluminium plate than with the PMMA plate ($\rho_6 \sim 0$) and, in return, that the rate of the

photoreaction, $\langle r_R \rangle$ could be increased. The experimental results presented in Fig. 4 show that, at identical irradiation times, higher conversions were obtained with the aluminium plate than with the PMMA, and are thus in agreement with these calculations. More generally, these findings point out that the reflection properties of the material of the base plate in which the tubing is fixed should imperatively be considered when modelling radiative transfer in microphotoreactors due to the short optical path lengths involved, which is not the case for large-scale photoreactors.

Determination of the incident photon flux density

The application of the revised model to experimental measurements allowed the incident photon flux density in the spiral-shaped microreactor, q_0 , to be determined. It was identified by minimizing the squared difference between the variation of the concentration of NCS predicted by the models described in Table 1 and the experimental one. For this, the following inlet parameters were considered:

- The inlet concentration of the Reinecke's salt, $C_{R,0}$, was 15 mol.m^{-3} ,
- The fraction of the non-irradiated volume, f_d , was null;
- The reflection coefficient at the interface N°6, ρ_6 , was taken equal either to that of aluminium $\rho_{Al} (= 0.900)$ or to that of PMMA $\rho_{PMMA} (= 0.039)$ [39].

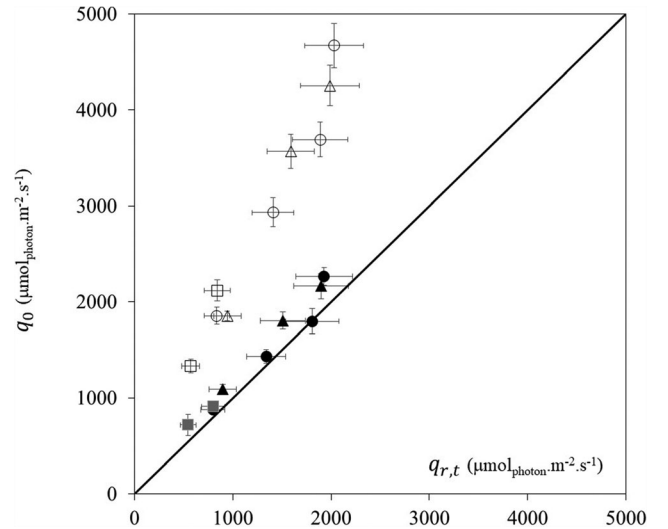


Fig. 9 Comparison between the predicted incident photon flux densities q_0 and $q_{r,t}$, deduced from Eq. 15 using the densities measured with the quantum sensor. Empty and full symbols correspond to the normal collimated emission and diffuse emission models, respectively. Circles are related to the yellow light emission mode, triangle to the blue light emission mode and square to the green light emission mode. Operating conditions: $d_i = 1 \text{ mm}$; aluminium base plate. The values associated with this figure are reported in Table S.3 of the Supplementary Material

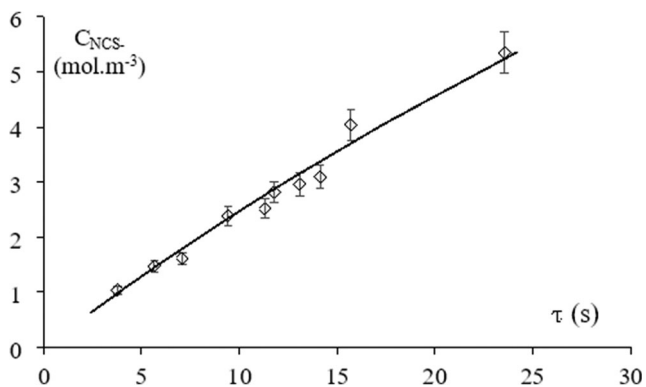


Fig. 10 Typical comparison between experimental (empty diamond) and predicted (line) conversions when a diffuse emission was considered in the modelling. Operating conditions: microreactors with $d_i = 1$ mm and the aluminium base plate; yellow light mode; $q_r = 32 \text{ mW.cm}^{-2}$; $q_0 = 1431 \text{ } \mu\text{mol}_{\text{photon.m}^{-2}.\text{s}^{-1}}$

In addition, it was assumed that the average optical path length, $\bar{\delta}$, was equal to the internal diameter, d_i (0.001 m) and that the specific irradiated surface, a_{light} , was equal to the inverse of the internal diameter (1000 m^{-1}).

Figure 9 presents the results found when considering the experimental data obtained with the different microreactors with $d_i = 1$ mm and the base plate in aluminium (the numerical values are reported in Table S.3 in the Supplementary Material). The incident photon flux densities were identified for each model (i.e. normal collimated and diffuse emissions). The uncertainties related to the identification process was estimated to $\pm 10\%$ (there were calculated by taking into account the distribution of experimental points around the model, see Fig. 10).

At this stage, it could be recalled that, to be consistent, the identified incident photon flux density, q_0 , should remain lower than or equal to the photon flux density measured at the inner surface of the microreactor, $q_{r,t}$, which thus corresponds to the maximal value that q_0 can take if the reflection coefficient at the interface N°2 (FED/reaction medium) is null ($\rho_2 = 0$). Reported in Fig. 9, $q_{r,t}$ is calculated from the following equation:

$$q_{r,t} = (1 - \rho_1)q_r \quad (15)$$

where ρ_1 is the reflection coefficient at the interface N°1 (air/FEP) and q_r is the photon flux density at the interface N°1 (air/FEP) (see Fig. 7). As shown in the Supplementary Material, ρ_1 is equal to 0.021 and to 0.068 for a normal collimated and a diffuse emission, respectively (see section S.5), and q_r can be considered equal to the photon flux density measured with the quantum sensor, q_r^{sensor} (see Table S.2).

From Fig. 9, it can be seen that, when a normal collimated emission is considered in the model, the values of q_0 are always significantly higher than those of $q_{r,t}$ (since the ratio $q_0/q_{r,t}$ approximately equal to 2.4). Thus, the

modelling with a normal collimated emission largely overestimates the values of q_0 . However, in keeping in mind that the relative standard deviation of values of q_r^{sensor} are almost 15%, the 1D model considering the diffuse emission gives acceptable values of q_0 , i.e. close to $q_{r,t}$ (and thus having an acceptable physical meaning).

The collimated model led to determine higher photon flux densities q_0 than those with the diffuse model. It is due to a classical feature of radiative transfer: for a given radiative configuration, the photon absorption probability (\mathcal{A}) is always lower with normal-collimated incident radiation (\mathcal{A}_C) than that with diffuse one (\mathcal{A}_D). In the identification process, the lower values of \mathcal{A}_C are compensated by high values of q_0 .

To sum up, when the real features of the LED array (diffuse emission, see Supplementary Material, section S.3), and of the microreactor (reflection by the base plate) are included in the modelling, the values of q_0 obtained from the actinometry method are in rather good agreement with the sensor measurements. In this case, the experimental variation of the concentration of NCS with the residence time can be well described by the model, as illustrated in Fig. 10.

Conclusion

In this paper, the implementation of the Reinecke's salt actinometer system suitable for the visible region was proposed in a LED-driven spiral-shaped microreactor. First, the revised protocol recently developed by Radjagobalou et al. [29] was successfully transferred to work under continuous-flow and with different irradiation conditions (three spectral domains, various emitted radiant powers), showing the adequacy of this method for characterizing continuous-flow microphotoreactors. Then, the experiments carried out showed that neither the length of the tubing nor the occurrence of Taylor flows with nitrogen bubbles had an influence on the photodissociation rate in the microfluidic device presented here. Finally, the one-dimensional Cartesian model (infinite parallel plates), classically used to extract the incident photon flux density from the experimental data was upgraded to account for the features of the LED-driven spiral-shaped microreactor, namely the diffuse emission and the reflection induced by the plate in which the tubing was inserted. It allowed the incident photon flux densities to be estimated with an acceptable level of accuracy. These findings offer promising perspectives for flow photochemistry applications, in particular to predict volumetric productivities.

Associated content

The Supporting Material includes the experimental protocol for actinometry measurements (section S.1), a description of the

spiral-shaped microreactor (section S.2) and the LED array (section S.3), the experimental investigations (section S.4), a description of the light path (section S.5), the calculation of $\langle E \rangle$ in the case of a normal collimated emission (section S.6), the calculation of $\langle E \rangle$ in the case of a diffuse emission (section S.7), and the estimation of the incident photon fluxes (section S.8).

Supplementary Information The online version contains supplementary material available at <https://doi.org/10.1007/s41981-021-00179-w>.

Acknowledgments This work was sponsored by the French Research Agency (ANR) under the Collaborative Research Project Programme PICPOSS (ANR 15 CE07 0008 01).

J. Dauchet, J. F. Cornet and F. Gros wish to thank the French National Agency as this work was sponsored by a public grant overseen by this Agency as part of the “Investissements d’Avenir” programme through the IMobS3 Laboratory of Excellence (ANR 10 LABX 0016) and the IDEX ISITE initiative CAP 20 25 (ANR 16 IDEX 0001).

References

- Hoffmann N (2008). *Chem Rev* 108:1052–1103
- Ciana CL, Bochet CG (2007). *Chimia* 61:650–654
- Bach T, Hehn JP (2011). *Angew Chem Int Ed* 50:1000–1045
- Zimmerman HE (1969). *Angew Chem Int Ed* 8(1):1–88
- Turro NJ (1986) Geometric and topological thinking in organic chemistry. *Angew Chem Int Ed* 25(10):882–901
- Hoffmann N (2012). *Photochem Photobiol Sci* 11(11):1613–1641
- Coyle EE, Oelgemöller M (2008). *Photochem Photobiol Sci* 7:1313–1322
- Oelgemöller M (2012). *Chem Eng Technol* 35(7):1144–1152
- Cambié D, Bottecchia C, Straathof NJW, Hessel V, Noël T (2016). *Chem Rev* 116(7):10276–11034
- Loubière K, Oelgemöller M, Aillet T, Dechy Cabaret O, Prat L (2016). *Chem Eng Process* 104:120–132
- Haas CP, Roider T, Hoffmann RW, Tallarek U (2019). *React Chem Eng* 4:1912–1916
- Braun AM, Peschl G, Oliveros E (2004) In: handbook of organic photochemistry and photobiology 3rd edn. CRC Press
- Aillet T, Loubiere K, Dechy Cabaret O, Prat L (2012). *Chem Eng Process* 64:38–47
- Cornet JF, Marty A, Gros JB (1997). *Biotechnol Prog* 13:408–415
- Braun AM., Maurette MT, Oliveros E (1986). *Photochemical technology*, J. Wiley & Sons. New York
- Kuhn H, Braslavsky SE, Schmidt R (2004). *Pure Appl Chem* 76:1–47
- Wriedt B, Ziegenbalg D (2020). *J Flow Chem* 10:295–306
- Aillet T, Loubiere K, Dechy Cabaret O, Prat L (2014). *Int J Chem React Eng* 12:1–13
- Hatchard CG, Parker CA (1956). *Proceedings of the Royal Society of London Series A, Mathematical and Physical Sciences* 235:518–536
- Wriedt B, Kowalczyk D, Ziegenbalg D (2018). *ChemPhotoChem* 2(10):913–921
- El Achi N, Bakkour Y, Chausset Boissarie L, Penhoat M, Rolando C (2017). *RSC Adv* 7:29815–29820
- Brauer HD, Schmidt R, Gauglitz G, Hubig S (1983). *Photochem Photobiol* 37(6):595–598
- Santos AR, Ballardini R, Belser P, Gandolfi MT, Iyer VM, Moggi L (2009). *Photochem Photobiol Sci* 8(12):1734–1742
- Rochatte V, Dahi G, Eskandari A, Dauchet J, Gros F, Roudet M, Cornet JF (2017). *Chem Eng J* 308:940–953
- Heller HG, Langan JR (1981). *J Am Chem Soc*:341–343
- Pitre SP, McTiernan CD, Vine W, Dipucchio R, Grenier M, Scaiano JC (2015). *Sci Rep* 5:1–10
- Roibu A, Franssen S, Lebleci E, Meir G, Van Gerven T, Kuhn S (2018). *Sci Rep* 8(1):5421
- Wegner EE, Adamson AW (1966). *J Am Chem Soc* 88(3):394–404
- Radjagobalou R, Blanco JF, da Silva Freitas VD, Supplis C, Gros F, Dechy Cabaret O, Loubière K (2019). *J Photochem Photobiol A* 382:111934
- Radjagobalou R, Blanco JF, Petrizza L, Le Behec M, Dechy Cabaret O, Lacombe S, Save M, Loubière K (2021). *ACS Sustain Chem Eng*. <https://doi.org/10.1021/acssuschemeng.0c06627>
- Mei M, Felis F, Dietrich N, Hébrard G, Loubière K (2020). *Theor Found Chem Eng* 54(1):25–47
- Mei M, Dietrich N, Hébrard G, Loubière K (2020). *Chem Eng Sci* 222:115717
- Yao C, Zhao Y, Maa H, Liu Y, Zhao Q, Chen G (2021). *Chem Eng Sci* 229:116017
- Radjagobalou R, Blanco JF, Dechy Cabaret O, Oelgemöller M, Loubière K (2018). *Chem Eng Process* 130:214–228
- Terao K, Nishiyama Y, Kakiuchi K (2014). *J Flow Chem* 4(1):35–39
- Nakano M, Nishiyama Y, Tanimoto H, Morimoto T, Kakiuchi K (2016). *Org Process Res Des* 20(9):1626–1632
- Nakano M, Morimoto T, Noguchi J, Tanimoto H, Mori H, Tokumoto SI, Koishi H, Nishiyama Y, Kakiuchi K (2019). *Bull Chem Soc Jpn* 92(9):1467–1473
- Telmesani R, White JAH, Beeler AB (2018). *ChemPhotoChem* 2:865
- M. N. Polyanskiy, “Refractive index database.” <https://refractiveindex.info/>

Publisher’s note Springer Nature remains neutral with regard to jurisdictional claims in published maps and institutional affiliations.